

SCIENTIFIC REPORTS



OPEN

Doubly Resonant Optical Periodic Structure

G. Alagappan & C. E. Png

Received: 05 October 2015

Accepted: 07 January 2016

Published: 08 February 2016

Periodic structures are well known in various branches of physics for their ability to provide a stopband. In this article, using optical periodic structures we showed that, when a second periodicity – very closed to the original periodicity is introduced, large number of states appears in the stopband corresponding to the first periodicity. In the limit where the two periods matches, we have a continuum of states, and the original stopband completely disappears. This intriguing phenomena is uncovered by noticing that, regardless of the proximities of the two periodicities, there is an array of spatial points where the dielectric functions corresponding to the two periodicities interfere destructively. These spatial points mimic photonic atoms by satisfying the standards equations of quantum harmonic oscillators, and exhibit lossless, atom-like dispersions.

Doubly resonant systems have compelling physical properties resulting from the interference effects. A three level atomic system with a Λ configuration has two resonant transitions, and by an appropriate coherent driving, we can generate steep positive (normal)^{1–4} and steep negative (anomalous)^{5–7} optical dispersions. Such steep dispersions can be exploited to create novel systems of slow light and subluminal light without any violation in the Einstein's causality principle^{8–9}. Steep positive dispersions are usually obtained in the three level systems using an electromagnetic induced transparency (EIT) setup^{1–3}, and there have been many proposals to mimic such configuration using plasmonic^{10–11} and optical^{12–15} double resonances. These mock versions work based on the coherent interference effects in the light scattering, and allow tuning of the positive dispersions via modifications in the geometrical structures. They also have been shown to possess scattering dark states¹⁶ and superscattering states^{17,18}. In this article, we demonstrate the intriguing optical properties of a new paradigm of doubly resonant systems that exploits structures with both short and long range spatial periodicities, and exhibiting two closely spaced Bragg resonances.

Typical periodic structures are single – period, structures (SPSs), and they exhibit stopbands [i.e., spectral regions for which wave propagations are forbidden]. The physical principle behind this stopband formation is the Bragg resonance of the SPS. Waves with frequency in the vicinity of Bragg resonance frequency, will experience a strong Bragg reflectivity, and therefore is unable to penetrate the bulk of the SPS.

In optics a SPS can be created by mean of a periodic variation of the dielectric constant with a fixed spatial period, a . We can again modulate the dielectric profile of this SPS, slowly and periodically, with a longer spatial period, a_s ^{19–21}. This new periodic structure which exhibits rapid, short range periodicity (a) and slow, long range periodicity (a_s) is defined as a dual periodic structure (DPS). Intuitively, one can expect in the limit of a very large a_s , the slow modulation vanishes, and consequently a DPS reduces to a SPS. However, a DPS in this limit does not fit into this simple intuition.

In the Fourier spectra, the dielectric function of a weakly modulated SPS, will exhibit one frequency peak at the fundamental spatial frequency $G = 2\pi/a$. However, for the DPS, due to the slow dielectric modulation, we will see a group of closely spaced peaks around the fundamental frequency. Assuming a DPS with only two of such closely spaced peaks (i.e., a structure with double Bragg resonances), the dielectric function can be casted as,

$$\varepsilon(x) = \varepsilon_0 + \varepsilon_1 \cos(Gx) + \varepsilon_1 \cos\left(\frac{G}{r}x\right) \quad (1)$$

where r is a number close to 1. In Eqn. 1, $\varepsilon_1 \ll \varepsilon_0$, and for a simplicity, we assumed the strengths of the two closely spaced harmonics to be equal (i.e., the amplitudes of two cosine functions in Eqn. 1 are equal). The conservation of translational symmetry in DPS requires $\varepsilon(x) = \varepsilon(x + a_s)$, and using Eqn. 1 it can be shown that this demands

Photonics and Plasmonics, Institute of High Performance Computing, Agency for Science, Technology, and Research (A-STAR), Singapore. Correspondence and requests for materials should be addressed to G.A. (email: gandhi@ihpc.a-star.edu.sg)

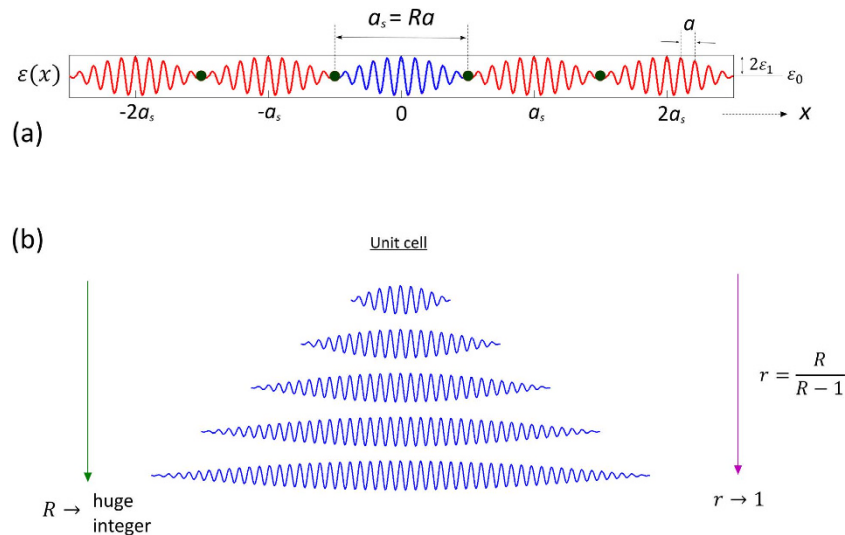


Figure 1. (a) Sketch of Eqn. 1 with $r = R/(R - 1)$. At the location of green dots we have $\varepsilon(x) = \varepsilon_0$. (b) Evolution of the DPS unit cell as a function of increasing R .

a_s/a to be the least integer multiple of r . The least integer multiple exist, only if r is rational. Assuming a rational r , and taking its' least integer multiple as R , we have $a_s = Ra$.

In a DPS, the mixing of the two harmonics, G and G/r creates the spatial “beats” in the dielectric function at a longer spatial scale. The length of the beat ($a_s = Ra$) is longer when the spacing between the two harmonics is closer. The closest allowed proximity between the two harmonics, G and G/r is one reciprocal lattice vector of the DPS, $g = 2\pi/a_s$. Any spacing lesser than g , is symmetrically forbidden, and hence will break the translational symmetry of the DPS. Assuming $r > 1$, and the spacing, $G - G/r = g$, it is easy to show that the rational form of r is $r = R/(R - 1)$ [or equivalently $R = r/(r - 1)$].

For a SPS, $r = 1$, and from Eqn. 1 we have $\varepsilon(x) = \varepsilon_0 + 2\varepsilon_1 \cos(Gx)$. For the DPS, a direct substitution of $r = 1$ for the limit $r \rightarrow 1$ in Eqn. 1 leads to a plausible inference that the DPS should be identical to the SPS in the limit $r \rightarrow 1$, and therefore recovers the original stopband of the SPS. However, the constraint $r = R/(R - 1)$ for the DPS prevents the direct substitution of $r = 1$ for the limit $r \rightarrow 1$ in Eqn. 1. The flawless method of analysing the limit $r \rightarrow 1$ in DPS is by letting R to take a huge integer value. As an illustration, Fig. 1(a) shows a sketch of $\varepsilon(x)$ with the unit cell from $-a_s/2$ to $a_s/2$ is highlighted in blue. Figure 1(b) depicts the evolution of the unit cell as R is increased to a huge integer value. As we can see from Fig. 1(a,b), regardless of the proximity of r to 1, the dielectric function of the DPS is topologically different from the dielectric function of the SPS – which is an unmodulated cosine function. As a signature difference, in DPS, the destructive interference between the two cosine waves in Eqn. 1 creates an array of spatial points (i.e., the green dots in Fig. 1) that are shielded from the effect of the rapid dielectric modulation with the period a . As we shall illustrate, this array of spatial points mimics an array of photonic atoms by satisfying the standard equations of quantum harmonic oscillators²². These photonic atoms create edge states (at the edge of the DPS unit cell) that closes the stopband due to the rapid dielectric modulation, despite the limit $r \rightarrow 1$. The dispersions in the vicinity of these photonic atoms, are strongly anomalous (i.e., a steep negative dispersion), and very much similar to the dispersions in mediums with inverted populations^{23–24} and gain doublets^{5–7}.

DPS as a Metamaterial Cavity

For the purpose of the numerical illustration, throughout this article, we use $\varepsilon_0 = 2.56$, and $\varepsilon_1 = 0.16$. An optical structure with such dielectric constants, and the dielectric profile as in Eqn. 1 with a large R , can be realized in many different ways. Some of the techniques include, fabrication of porous silicon via electrochemical anodization with varying current density²⁵, deposition of a dual periodic multilayer using a logical combination technique¹⁹, holographic interferometry, that make uses laser beam interferences on photosensitive materials²⁶, and the deposition of silicon oxynitride with varying stoichiometry of oxygen and nitrogen^{27–28}.

Using a plane wave expansion method²⁹, we can solve the dispersion relation, $\omega = a/\lambda$ versus k , where ω , λ and k are the normalized frequency, freespace wavelength and wavevector, respectively. Firstly, consider the limiting case, when $r \rightarrow 1$. As $r = R/(R - 1)$, the dispersion curve of the DPS in this limit can be obtained asymptotically by increasing R to a huge integer value, using an extended zone scheme³⁰. For a very large R , the dispersion of the DPS converges to a continuous curve, $\Omega(k)$, shown in Fig. 2(a) [blue curve]. In the same diagram, we have also plotted the dispersion curves of the SPS, and a homogenous medium with dielectric constant ε_0 . When $r \rightarrow 1$, from the direct substitution of $r = 1$ in Eqn. 1, one can expect the dispersion of the DPS to be identical to the dispersion of the SPS. However, this is only true for wavevectors far from $G/2$. For wavevectors far from $G/2$, both SPS and DPS behave as linear homogenous materials of dielectric constants ε_0 . Near $k = G/2$, the dispersion relation of the DPS is remarkably different from the dispersion relation of the SPS despite $r \rightarrow 1$ [Fig. 2(a)]. In the SPS, the

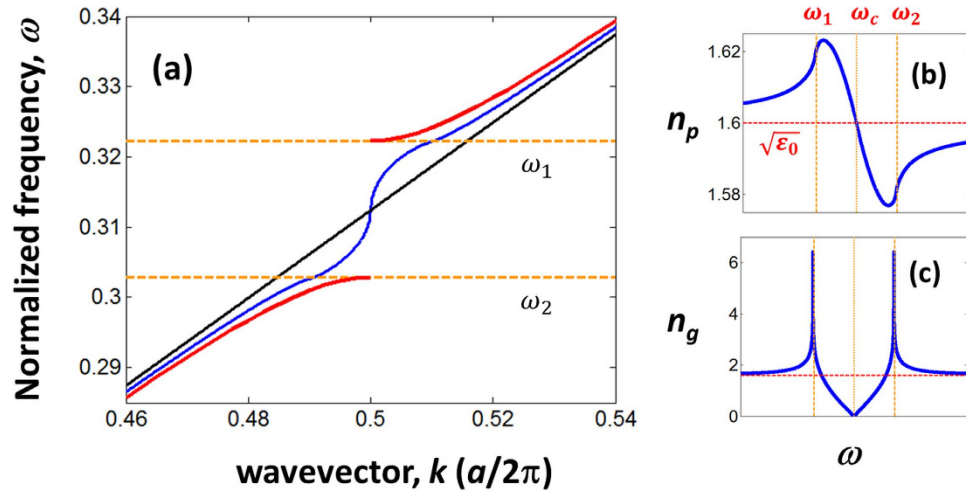


Figure 2. (a) Dispersion curves. Black – Homogenous medium with the dielectric constant ϵ_0 , Red – SPS, Blue – DPS in the limit $r \rightarrow 1$. (b) Refractive index, $n_p(\omega)$ for the DPS in the limit $r \rightarrow 1$. (c) Group index $n_g(\omega)$ for the DPS in the limit $r \rightarrow 1$. In (b,c), the dashed vertical lines represent the SPS stopband edges (ω_1 and ω_2), and the stopband centre (ω_c). The dashed horizontal lines in (b,c) correspond to the refractive index, $\sqrt{\epsilon_0}$.

dispersion is discontinuous at $k = G/2$, and consequently we have a stopband between the frequencies $\omega_c(1 - \frac{\epsilon_1}{2\epsilon_0})$ and $\omega_c(1 + \frac{\epsilon_1}{2\epsilon_0})$, where $\omega_c = \frac{1}{2\sqrt{\epsilon_0}}$ is the stopband centre²⁹. In the DPS this stopband completely closes, and the dispersion relation takes a continuous, sigmoid shape curve around ω_c . Thus, in the vicinity of ω_c , the DPS with $r \rightarrow 1$, can be characterized with a dispersive refractive index, $n_p(\omega)$. This refractive index can be defined via the phase index definition as $n_p(\omega) = \frac{1}{G} \frac{k}{\Omega(k)}$, and the corresponding plot as a function of frequency is shown in

Fig. 2(b). From this figure, we can see that $n_p(\omega)$ exhibits a large normal dispersion (i.e., a positive $\frac{dn_p}{d\omega}$) near the stopband edges of the SPS. However, near $\omega = \omega_c$ the dispersion is strongly anomalous (i.e., negative $\frac{dn_p}{d\omega}$). In order

to better quantify the dispersion of the DPS with $r \rightarrow 1$, let's define a group index via $n_g(\omega) = \frac{1}{G} \frac{dk}{d\omega}$. Note that n_g is inversely proportional to the slope of the dispersion curve $[\Omega(k)]$, and its relationship with n_p can

be casted as $n_g = n_p + \omega \frac{dn_p}{d\omega}$. Figure 2(c) shows the plot of n_g as a function of frequency, and as we can see from this figure $n_g = n_p \approx \sqrt{\epsilon_0}$ for frequencies far away from the two SPS stopband edges. For frequencies near the stopband edges of the SPS, n_p exhibits a large normal dispersion [Fig. 2(b)], and consequently we have a subluminal group index with $n_g \gg n_p$ [Fig. 2(c)]. On the other hand, near $\omega = \omega_c$ the n_p exhibits a large anomalous dispersion, and consequently this gives a superluminal group index $n_g \approx 0$ [Fig. 2(c)]. The anomalous dispersion, and the resulting superluminal group index of the DPS in the limit $r \rightarrow 1$, is very much similar to anomalous dispersions in the nonlinear mediums with population inversions^{23–24}, and gain doublets^{5–7}. Besides these active nonlinear structures, anomalous dispersion has been also shown as a result of scattering in passive structures that facilitates tunnelling of light^{8–9,31–34}. However, such system is very lossy since the anomalous dispersion is for the evanescent solution of the system. On the other hand, in the case of DPS (with the limit $r \rightarrow 1$), the anomalous dispersion is for the real solutions (i.e., propagating waves) of the system.

The refractive indices (n_p and n_g) obtained for the limit $r \rightarrow 1$ is indeed useful to describe and infer the behaviour of the DPSs with finite values of R . For a finite R , the DPS behaves like a multimode optical cavity made of an artificial material with the dispersive refractive index $n_p(\omega)$. For an illustration, in Fig. 3(a), we show the dispersion curve for $R = 500$. As we can see from this figure, the dispersion curve for $R = 500$, which is in similar shape as $\Omega(k)$ [Fig. 2(a)], is discontinuous at each half of the Brillouin zone (BZ), forming discrete bands in the vicinity of ω_c . Importantly, these discrete bands are flat, signifying the dispersions of slow or localized optical modes³⁵. The dispersion curve for $R = 500$ in the reduced zone scheme is shown in Fig. 3(b). Note that, the dispersion curve in the reduced zone scheme is better known in the name of photonic band structure^{29,36}. In Fig. 3(c–f), we show the photonic band structures for $R = 750, 1000, 2000$, and 5000 . The frequency positions of the flat bands, to a very good approximation is given by

$$\omega_m = \Omega\left(k = \frac{G + mg}{2}\right), \quad (2)$$

where m is a integer that indexes the flat band in the photonic band structure. The indexing scheme is shown in Fig. 3(b). The frequency spacing between the flat bands, $\Delta\omega$, can be expressed using the group index of the DPS in the limit $r \rightarrow 1$ [$n_g(\omega)$] as

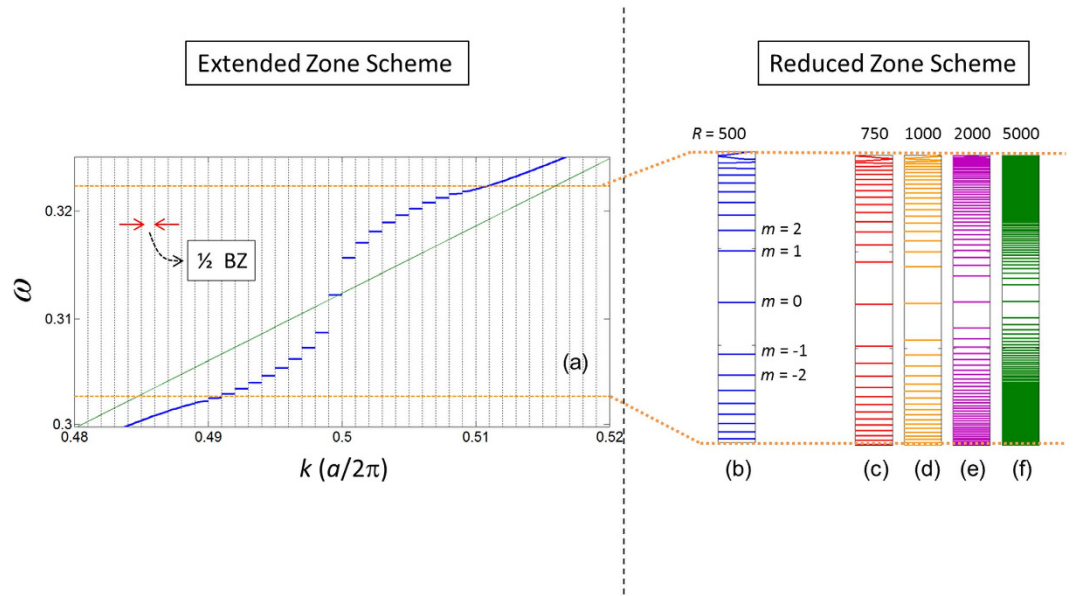


Figure 3. (a) Blue – dispersion curve of the DPS with $R = 500$ in the extended zone scheme. Green – dispersion curve of a homogenous medium. (b–f) Dispersion curves in the reduced zone scheme (i.e., photonic band structure) for $R = 500, 750, 1000, 2000,$ and 5000 . The horizontal axes in (b–f) represent wavevectors in the half of the BZ. The photonic band structure is obtained by folding the dispersion curve in the extended zone scheme into the half of the BZ. The dashed orange lines indicate the band edges of the SPS. The label m in (b) represents the frequency subscript as in ω_m .

$$\Delta\omega = \frac{1}{2n_g(\omega)R}. \tag{3}$$

This frequency spacing for the DPS with the finite R is the same as the frequency spacing in a Fabry Perot cavity made with a dispersive dielectric material of refractive index $n_p(\omega)$, with a length Ra . From Fig. 3(b–f), we can see that the density of the flat bands increases as a function of R . This is because the discretization step (i.e., the length of half BZ $=g/2 = \pi/Ra$) decreases as R increases. Further, these figures also indicate that the density of flat bands are not uniform across the frequencies of the stopband. For each R in Fig. 2(b–f), the density of flat bands is maximum near SPS band edge frequencies, and the density is minimum near the SPS stopband centre. These density variations are due the dispersive nature of $n_p(\omega)$, and can be easily understood from the frequency spacing [Eqn. 3] which is inversely proportional to $n_g(\omega)$. The values of $n_g(\omega)$ are maximum and minimum for SPS stopband edges and stopband centre, respectively [see the n_g plot in Fig. 2(c)]. Therefore, the densities of flat bands are maximum and minimum for frequencies near SPS stopband edges and stopband centre, respectively.

DPS as a Photonic Harmonic Oscillator

In order to perceive the intriguing dispersion of the DPS, let us examine the dielectric function in the vicinity of green dots in Fig. 1. For the sake of discussion let us pick $x = a_s/2$. Using the approximation $\sin \theta \approx \theta$ for a small angle θ , it can be easily shown that near $x = a_s/2$, and for a large R Eqn. 1 becomes $\varepsilon(x) = \varepsilon_0 - \varepsilon_1 \left[x - \frac{a_s}{2} \right] \sin Gx$. As can be seen from this equation, in the proximity of $x = a_s/2$, the strength of the rapid dielectric modulation—the modulation with the period a (i.e., the amplitude of $\sin Gx$) is $\varepsilon_1 \left[x - \frac{a_s}{2} \right]$, and it is a linear function of x .

When x is exactly $\frac{a_s}{2}$, the strength of the rapid dielectric modulation is zero, and we have $\varepsilon(x) = \varepsilon_0$. This means, at this position the DPS is completely shielded from the effect of the SPS (i.e., the rapid dielectric modulation). So, any light with a frequency in the vicinity of the SPS stopband centre (i.e., $\omega = \omega_c$) tends to concentrate at $x = \frac{a_s}{2}$. A slight deviation from $x = \frac{a_s}{2}$, causes the light to face the rapid dielectric modulation of the SPS in a linearly increasing strength, $\varepsilon(x) = \varepsilon_0 - \varepsilon_1 \left[x - \frac{a_s}{2} \right] \sin Gx$, and as a consequence the light will be reflected back towards $x = \frac{a_s}{2}$. As the stopband resulting from the rapid dielectric modulation, is proportional to the strength of the modulation $\varepsilon_1 \left[x - \frac{a_s}{2} \right]$, the reflection will be stronger as the deviation from $x = \frac{a_s}{2}$ increases. As we shall prove in the following, this scenario is analogous a lossless harmonic oscillator with linearly increasing restoring force³⁰.

In order to analyse the localized modes at $x = \frac{a_s}{2}$, let us first move the origin of the x -axis from 0 to $\frac{a_s}{2}$. In the new coordinate system, Eqn. 1 becomes $\varepsilon(x) = \varepsilon_0 - 2\varepsilon_1 \sin \frac{Gx}{2} \sin \frac{Gx}{2} \left(1 + \frac{1}{r} \right) \cos \pi R$. Near $x = 0$, assuming an even R , we have $\varepsilon(x) = \varepsilon_0 - \varepsilon_1 g x \sin G_r x$, where $G_r = \frac{G}{2} \left(1 + \frac{1}{r} \right)$. In Fig. 4(a), we illustrate $\varepsilon(x)$, and its slowly varying amplitude functions in the new coordinate system. As we can readily see from this figure, $\varepsilon_1 g x$ provides a very good approximation to the slowly varying amplitude over half of the unit cell [i.e., from $-a_s/4$ to

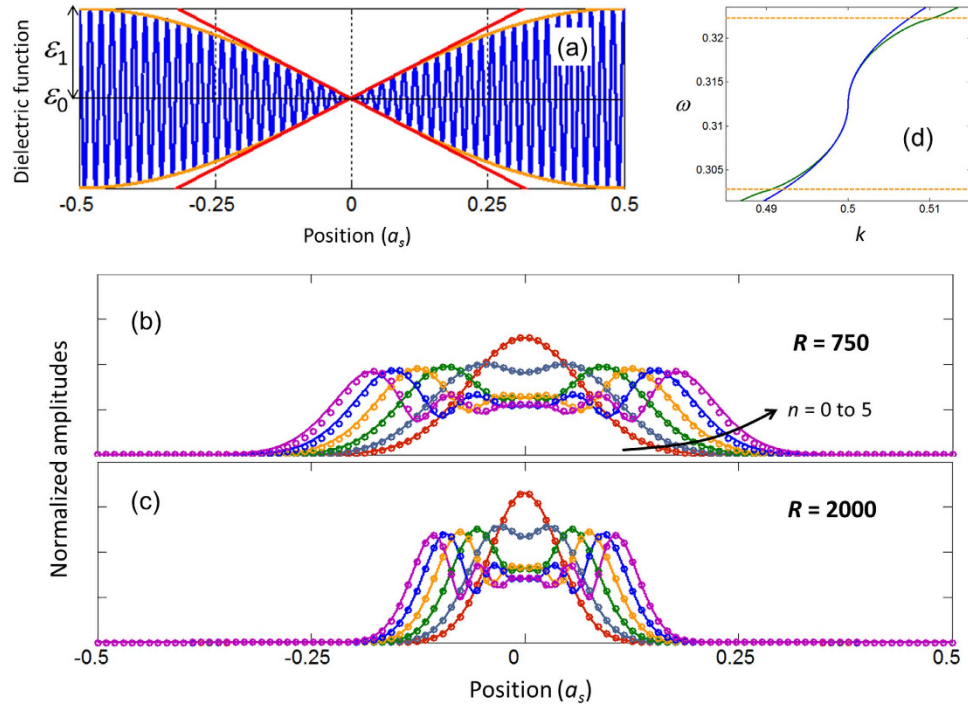


Figure 4. (a) Blue – the dielectric function of the DPS, $\varepsilon(x) = \varepsilon_0 - 2\varepsilon_1 \sin \frac{gx}{2} \sin \frac{Gx}{2} \left(1 + \frac{1}{r}\right)$. Orange – the slowly varying amplitude of $\varepsilon(x)$, $\varepsilon_0 - 2\varepsilon_1 \sin \frac{gx}{2}$. Red – the slowly varying amplitude of $\varepsilon(x)$ near $x = 0$, $\varepsilon_0 - \varepsilon_1 gx$. (b,c) Normalized electric field amplitudes for the localized modes ($n = 0$ to 5) of the DPS. Circles – analytical calculations via Eqn. 14. Solid line – exact numerical calculations. (d) The dispersion curves in the limit $r \rightarrow 1$. Blue – analytical calculation via Eqn. 15. Green – exact numerical calculation (same as the blue curve in Fig. 2).

$a/4$]. With $\varepsilon(x) = \varepsilon_0 - \varepsilon_1 gx \sin G_r x$, the time-independent Maxwell’s equation for the light in the DPS can be written as,

$$\frac{d^2 E(x)}{dx^2} + \omega^2 G^2 [\varepsilon_0 - \varepsilon_1 gx \sin G_r x] E(x) = 0, \tag{4}$$

where $E(x)$ is the electric field. In order to solve Eqn. 4, assume the DPS to be a SPS with a linearly perturbed dielectric function in the slow spatial scale. Consequently, $E(x)$ can be expressed as a linear combination of the SPS’s modes,

$$E(x) = p(x) \cos \frac{G_r}{2} x + q(x) \sin \frac{G_r}{2} x, \tag{5}$$

where $\cos \frac{G_r}{2} x$ and $\sin \frac{G_r}{2} x$ are the modes of the SPS which are rapidly varying functions. The coefficients $p(x)$ and $q(x)$ are slowly varying functions. Substituting Eqn. 5 into Eqn. 4, and applying a slowly varying envelope approximation³⁷, we can average out the rapidly varying terms. The resulting slow scale equations are coupled equations,

$$\frac{dp}{dx} = -\alpha p x + \beta q, \tag{6}$$

$$\frac{dq}{dx} = \alpha q x - \beta p, \tag{7}$$

where $\alpha = \frac{\omega^2 G^2 \varepsilon_1}{2R - 1}$, and $\beta = \frac{G^2 \varepsilon_0}{G_r} [\omega^2 - \omega_{0r}^2]$ are frequency dependant constants. Here,

$$\omega_{0r} = \frac{\omega_c}{2} \left(1 + \frac{1}{r}\right), \tag{8}$$

with $\omega_c = \frac{1}{2\sqrt{\varepsilon_0}}$ is the center of SPS bandgap. Changing the variable, x , to a dimensionless position variable, $z = x\sqrt{\alpha}$, and eliminating q and p in Eqns 6 and 7, respectively, we have two independent second order differential equations,

$$\frac{d^2p}{dz^2} + \left[\frac{\beta^2}{\alpha} + 1 - z^2 \right] p = 0, \tag{9}$$

$$\frac{d^2q}{dz^2} + \left[\left(\frac{\beta^2}{\alpha} - 2 \right) + 1 - z^2 \right] q = 0. \tag{10}$$

Eqns 9,10 mimic the standard Schrodinger equation for a quantum harmonic oscillator, $\frac{d^2\psi_n}{dz^2} + [2n + 1 - z^2]\psi_n = 0$ with n being a non-negative integer. The solution for the Schrodinger equation is $\psi_n(z) = (2^n n! \sqrt{\pi})^{-1/2} e^{-z^2/2} H_n(z)$, where $H_n(z)$ is the Hermite polynomial of order n ³⁸. Therefore, to solve Eqns 9,10, we let $\frac{\beta^2}{\alpha} = 2n$, and substituting the frequency expressions for α and β , gives us,

$$\omega^2 \pm \omega \sqrt{\frac{n\varepsilon_1}{R\varepsilon_0^2}} - \omega_{0r}^2 = 0. \tag{11}$$

Assuming $\omega_{0r}^2 \gg \sqrt{\frac{n\varepsilon_1}{R\varepsilon_0^2}}$, the positive solutions to Eqn. 11 are $\omega_{\pm n} = \omega_{0r} \pm \frac{1}{2} \sqrt{\frac{n\varepsilon_1}{R\varepsilon_0^2}}$. In order, to be consistent with the frequency indexing scheme used in Fig. 3(b), this solution also can re-written for any integer m as,

$$\omega_m = \omega_{0r} + \frac{1}{2} \text{sign}(m) \sqrt{\frac{|m|\varepsilon_1}{R\varepsilon_0^2}}, \tag{12}$$

where $\text{sign}(m) > 0$ and $\text{sign}(m) < 0$ for positive and negative values of m , respectively.

As we have let, $\frac{\beta^2}{\alpha} = 2n$ in Eqn. 9, we have $\frac{\beta^2}{\alpha} - 2 = 2(n - 1)$ for Eqn. 10. Thus, for a non-negative $n - 1$, we need $n \geq 1$, and consequently for $n = 0$ we have $p = \psi_0(z)$ and $q = 0$. For $n \geq 1$, the solutions for p and q in Eqns 9,10 can be written as $A\psi_n(z)$, and $B\psi_{n-1}(z)$, respectively. Here, A and B are constants, and using Eqns 6 and 11, it can be shown that they satisfy $A = B$ for $\omega = \omega_n$, and $A = -B$ for $\omega = \omega_{-n}$. With the solutions for $p(x)$ and $q(x)$, and the normalization condition $\frac{1}{a_s} \int_{-a_s/2}^{a_s/2} \varepsilon(x) E_n^2(x) dx = 1$, the electric fields [Eqn. 5] for the modes with frequencies $\omega_{\pm n}$ can be succinctly written as

$$E_{\pm n}(x) = \left[\frac{a_s}{2^{n-\rho} n! \varepsilon_0} \sqrt{\frac{\alpha}{\pi}} \right]^{\frac{1}{2}} e^{-\frac{\alpha x^2}{2}} \left\{ H_n(x\sqrt{\alpha}) \cos \frac{G_r x}{2} \pm \sqrt{2n} H_{n-1}(x\sqrt{\alpha}) \sin \frac{G_r x}{2} \right\}, \tag{13}$$

where $\rho = 1$ and 0 , for $n = 0$ and $n \geq 1$, respectively. As α is real and positive, the modes described by Eqn. 13 exhibit Gaussian evanescent tails, $e^{-\frac{\alpha x^2}{2}}$, which decay smoothly.

Eqn. 13 also can be written as $E_{\pm n}(x) = S_n(x) \cos \left[\frac{G_r x}{2} \pm \theta(x) \right]$, where $S_n(x)$ and $\theta(x)$ are the slowly varying amplitude and phase, respectively. From Eqn. 13, we can show that,

$$S_n(x) = \left[\frac{a_s}{2^{n-\rho} n! \varepsilon_0} \sqrt{\frac{\alpha}{\pi}} \right]^{\frac{1}{2}} e^{-\frac{\alpha x^2}{2}} \sqrt{H_n^2(x\sqrt{\alpha}) + 2nH_{n-1}^2(x\sqrt{\alpha})}. \tag{14}$$

For $n = 0$, $H_0(x\sqrt{\alpha}) = 1$, and we have Gaussian function for $S_0(x)$. In Fig. 4(b) we plot $S_n(x)$ using Eqn. 14 for $n = 0$ to 5, and $R = 750$. In the same figure, we have also plotted the similar quantity obtained from the exact numerical calculation (based on the plane wave expansion method²⁹). Figure 4(c) shows a similar plot to Fig. 4(b), however for $R = 2000$. As we can see from these figures, both analytical and exact calculations are in very good agreement. The degree of agreement reduces when the slowly varying electric field amplitude moves far from the centre of the DPS's unit cell.

In order to determine the continuous dispersion relation in the limit $r \rightarrow 1$, let us write the wavevector in the extended zone scheme as $k = \frac{G}{2} \pm n\frac{g}{2}$. Using this k , and the frequency expression, $\omega = \omega_{0r} \pm \frac{1}{2} \sqrt{\frac{n\varepsilon_1}{R\varepsilon_0^2}}$, it can be shown that, in the vicinity of ω_c and $r \rightarrow 1$, the dispersion curve of the DPS is defined by

$$k = \frac{G}{2} \left[1 \pm \frac{\varepsilon_0}{\varepsilon_1} \left(\frac{\omega - \omega_c}{\omega_c} \right)^2 \right]. \tag{15}$$

In Fig. 4(d), we compare the dispersion curve obtained from Eqn. 15, with respect to the exact numerical calculation (i.e., the blue curve in Fig. 2). As we can see from this figure, we have a good agreement between these two curves for frequencies in the stopband of the SPS, and in the vicinity of ω_c , the agreement is perfect. The discrepancies in the wavevector values of the analytically obtained curve with respect to the numerically evaluated curve

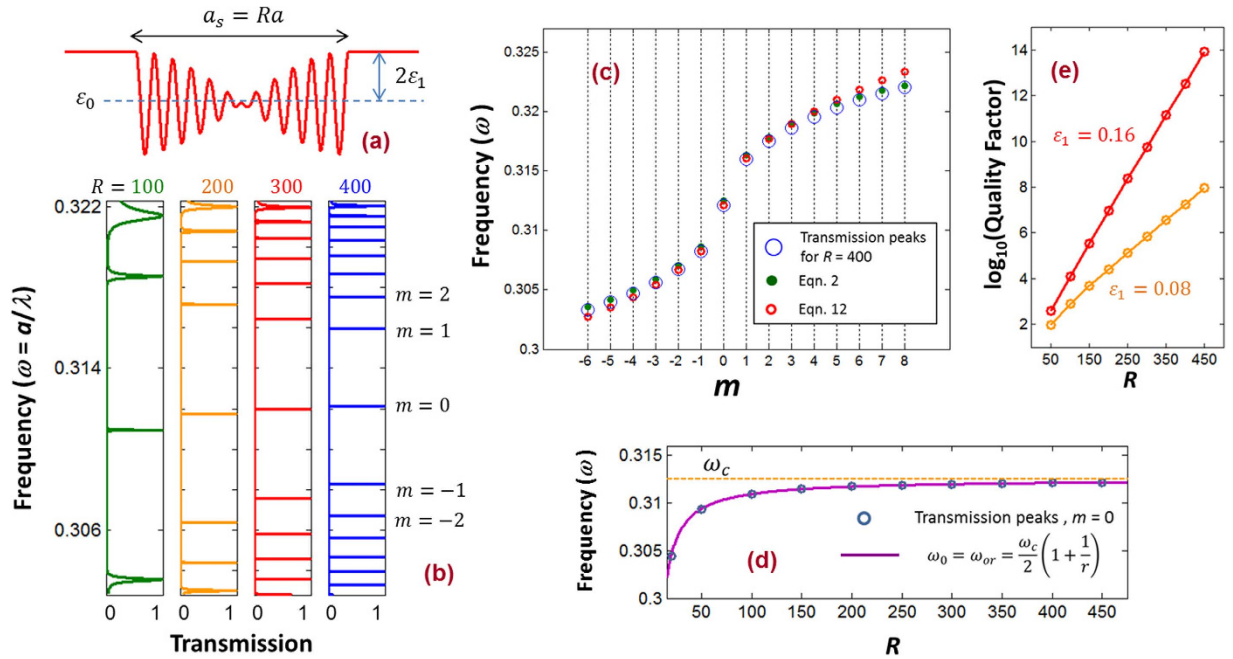


Figure 5. (a) Schematic of the single unit cell DPS. (b) Transmission spectrums for $R = 100, 200, 300$ and 400 . (c) (blue-open circles) Frequencies of transmission peaks for $R = 400$ from “(b)”, and frequencies from Eqn. 2 (green-closed circles), and Eqn. 12 (red-open circles). (d) Frequencies of $m = 0$ transmission peaks obtained from full numerical simulations (blue circles), and frequencies from the harmonic oscillator theory for $m = 0$ (solid purple line). (e) logarithmic value of the quality factors for $m = 0$ peaks as a function of R .

are less than 0.01% and 1% for frequencies near ω_0 and near the stopband edge, respectively. From Eqn. 15, the closed form expression of the refractive index is $n_p(\omega) = \frac{1}{2\omega} \left[1 \pm \frac{\varepsilon_0}{\varepsilon_1} \left(\frac{\omega - \omega_c}{\omega_c} \right)^2 \right]$. The group index can be obtained by differentiating Eqn. 15 with respect to ω as $n_g = \pm \frac{\varepsilon_0}{\varepsilon_1} \left(\frac{\omega - \omega_c}{\omega_c^2} \right)$. As we can see from this expression, for $\omega \rightarrow \omega_c$, we have $n_g \rightarrow 0$. This zero group index signifies that the light propagation in the vicinity of the equilibrium position [$x = 0$ (new coordinate system) in Fig. 4(a); green dot in Fig. 1(a)] is essentially a tunnelling process, and therefore superluminal in nature^{8–9,31–34}.

Application and Optical Performances of DPS

DPSs can be used for designing high quality broadband, and multichannel slow light devices. The harmonic modes of the DPS exhibit Gaussian evanescent tails, which decay smoothly. Therefore it naturally generates resonant peaks of high quality factors³⁹, despite of a geometrical structure with a low refractive index contrast. This is favourable for many applications such as high temperature realization of Bose-Einstein condensation of exciton polaritons⁴⁰, and realization low threshold nonlinear optical devices, using the abundant low refractive index optical materials.

In the metamaterial cavity section, we showed that for a finite R , the DPS exhibits many flat bands (for example see Fig. 3). In the transmission spectrum, these flat bands will appear as sharp resonant peaks. Figure 5(a) shows the schematic of a single unit cell DPS ($N = 1$). This single unit cell DPS acts as a metamaterial cavity. The dielectric constant of the ambience is taken as $\varepsilon_0 + 2\varepsilon_1$ to match with the dielectric constant at the edge of the unit cell [Fig. 5(a)]. The device with the schematic as shown in Fig. 5(a) can be easily fabricated using the holographic interferometric techniques²⁶. Figure 5(b) shows the simulated transmission spectrums [see the Methods section for the details of the numerical simulation] of the single unit cell DPS for $R = 100, 200, 300$, and 400 . The frequency window in this figures spans the entire bandgap window of the SPS [i.e., ω_1 to ω_2 ; see Fig. 2(a)]. As we can from this figure, the transmission spectrums of the DPS exhibit many sharp resonant peaks, and the number of peaks increases as R increases. The density of the transmission peaks are high and low near the bandgap edge and bandgap centre of the SPS, respectively. These observations are consistent with the band structure calculations [see section on the metamaterial cavity]. The density of the transmission peaks also agrees with the equation describing the frequency spacing of the flat bands [Eqn. 3].

Each sharp transmission peak in Fig. 5(b), can be labelled with an integer m using the frequency indexing scheme used in Fig. 3(b). We showed the frequency labelling for the transmission peaks of $R = 400$ in Fig. 5(b). This labelling will assist us to compare the locations of simulated transmission peaks with the theory developed in this paper. Figure 5(c) compares the positions of the transmission peaks with the resonant frequencies obtained from Eqn. 2 [i.e., from the continuous dispersion curve: blue curve in Fig. 2(a)] and Eqn. 12 [i.e., from the theory of photonic harmonic oscillators]. As the figure suggests, both of these frequency expressions serve as good approximations to the frequencies of the transmission peaks.

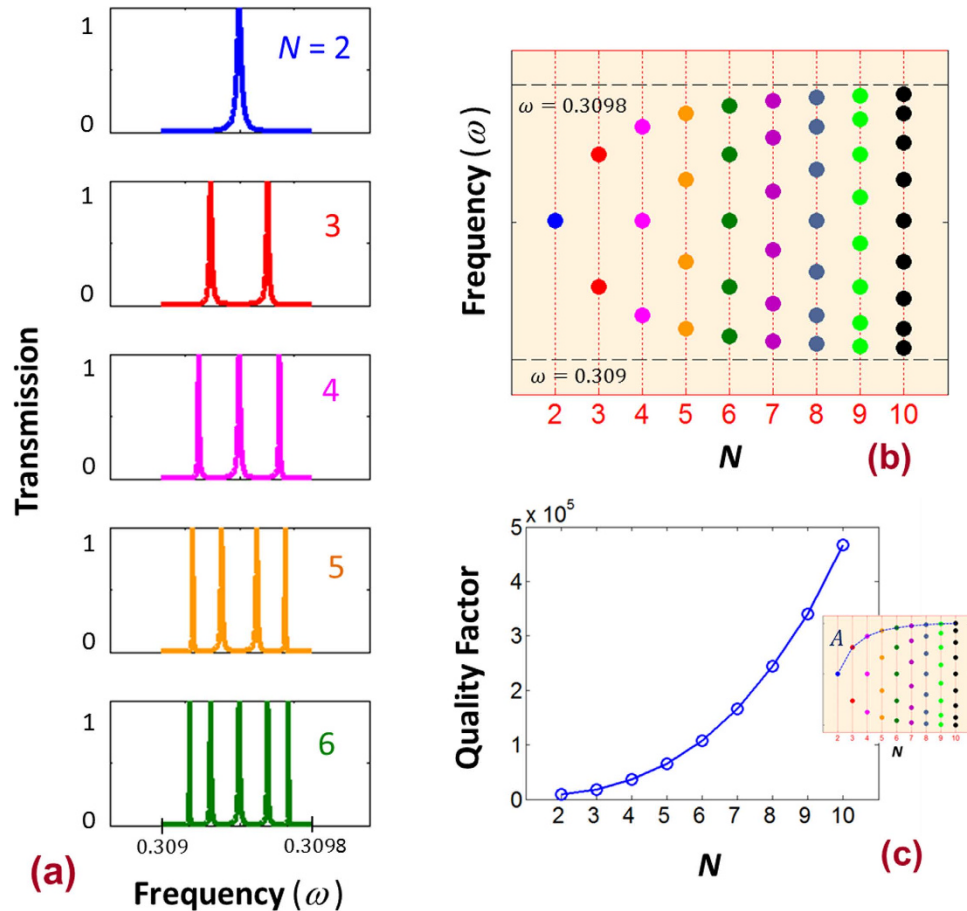


Figure 6. (a) Transmission peaks of a DPS ($R = 50$) with N unit cells that corresponds to $m = 0$ flat band (b) Frequencies of $m = 0$ band as a function of N . The $m = 0$ flat band has a frequency span of $\omega = 0.309$ to 0.3098 . (c) The quality factors of the transmission peaks along the path A (see the insert).

The most profound transmission peak of the DPS is the peak with $m = 0$. This peak has the highest quality factor, and the peak is visible even for small values of R . In Fig. 5(d), we plotted the frequency of the $m = 0$ resonant transmission peak (obtained with the full numerical simulation; see the Methods section) as a function of R . As R increases the frequency of the $m = 0$ peak move towards to the centre of the SPS bandgap, ω_c . The position of the $m = 0$ transmission peak is in perfect agreement with the prediction of the harmonic oscillator theory which gives $\omega_0 = \omega_{0r} = \frac{\omega_c}{2} \left(1 + \frac{1}{r}\right)$ [Eqns 8 and 12]. The plot ω_{0r} is shown in purple color in Fig. 5(d) for the continuous scale of R . As $R \rightarrow \infty$, we have $r \rightarrow 1$, and therefore $\omega_0 = \omega_{0r} \rightarrow \omega_c$. In order to assess the quality of transmission peaks with $m = 0$, in Fig. 5(e), we plot the logarithmic values of their quality factors as a function of R , for ε_1 values of 0.16 and 0.08. As we can see from this figure, the quality factor increases exponentially as R increases, and the quality factor is comparatively high when the dielectric modulation is of the DPS is high.

For $N > 1$ the finite DPS is indeed a coupled system of harmonic oscillators [Fig. 1]. An essential nature of any coupled oscillators is the splitting of the resonant peaks^{41–42}. The DPS with $N > 1$, and $\varepsilon_1 = 0.16$ [the schematic is shown in Fig. 1] is numerically simulated using an ambient dielectric constant of ε_0 [see the Methods section for the details]. Figure 6(a) shows the resulting transmission spectrum near the frequency ω_{0r} for $N = 2, 3, 4$ and 5 . When $N = 2$, there is one transmission peak with frequency of ω_{0r} . This peaks corresponds to the localized mode of $m = 0$, in the vicinity of one green dot in Fig. 1. When $N = 3$, there are two of such modes couples together, and as a result the original peak at $N = 2$ splits in two peaks [see Fig. 6(a)]. In general, for the DPS with N unit cells, the coupling of modes in adjacent oscillators results in $N-1$ closely spaced peaks. The splitting of the peaks is systematically depicted in Fig. 6(b). The frequency span of these closely spaced peaks equal to the bandwidth of the $m = 0$ flat band of the infinite system ($N \rightarrow \infty$), and the span can be obtained from the DPS band structure calculations. For $R = 50$, and $\varepsilon_1 = 0.16$ the frequency span obtained from the band structure calculation is from $\omega = 0.309$ to 0.3098 . If we choose to work around the telecommunication wavelength, then, for $a = 480$ nm, this normalized frequencies translates to wavelengths from 1549 to 1553 nms. This frequency span is adjustable. If we would like to have a narrow frequency span, then R has to be increased to generate a flatter band.

The closely spaced peaks for any given N in Fig. 6(a) display non-uniform quality factors. The outermost peak [see Fig. 6(a,b)] exhibits the largest quality factor. In Fig. 6(c), we show the quality factor of the outermost peak

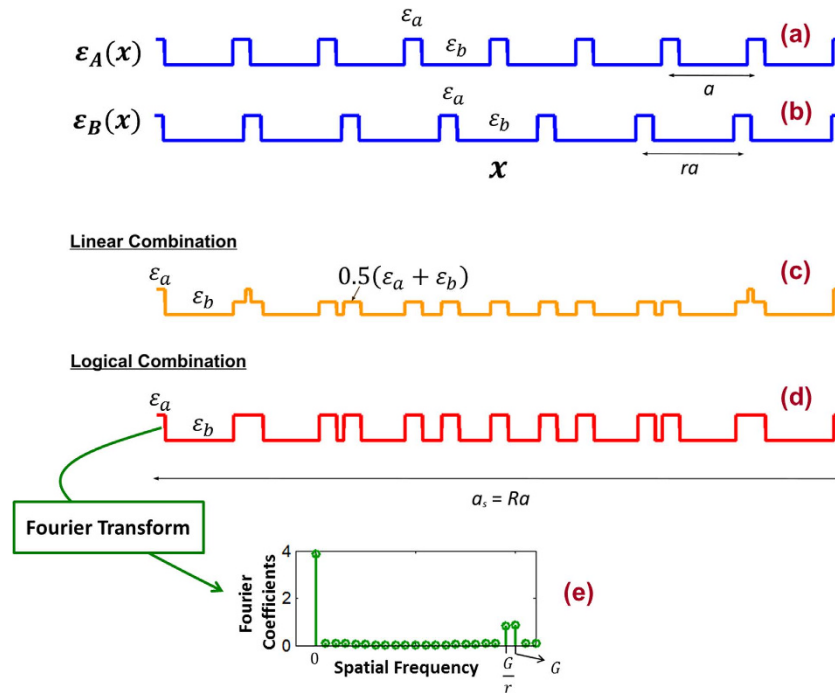


Figure 7. (a) Binary valued periodic dielectric function $[\varepsilon_A(x)]$ with period, a . (b) Binary valued periodic dielectric function $[\varepsilon_B(x)]$ with period, ra . (c) Linear combination of $\varepsilon_A(x)$ and $\varepsilon_B(x)$, $0.5\{\varepsilon_A(x) + \varepsilon_B(x)\}$. (d) Logical “OR” combination of $\varepsilon_A(x)$ and $\varepsilon_B(x)$ [ε_a and ε_b are treated as binaries 1 and 0, respectively] (e) Fourier transform of the periodic dielectric function (period = a_s) in “(d)”. Here, we assumed $\varepsilon_a = 3.4$ (silicon), $\varepsilon_b = 1.45$ (silicon dioxide), and the length of the ε_a portion within each period of $\varepsilon_A(x)$ and $\varepsilon_B(x)$ as $0.2a$.

[i.e., along the line A - insert of Fig. 6(c)] as a function of N . As N increases, the quality factors increases quadratically. Note this increase of quality factor with respect N is slower than the increase of quality factor with respect R , which is at the exponential scale [Fig. 5(e)].

Constructing a high dielectric contrast DPS

As we have mentioned in the metamaterial cavity section, the DPS with the dielectric function as in Eqn. 1 can be implemented in many different ways^{25–28}. Most of these methods generates continuous dielectric profile, and therefore they have two important limitations: 1) generating structures with large dielectric modulations (i.e., large ε_1); 2) generating structures that are amenable for mass production via lithographical techniques. Therefore, in this section, we would like to introduce the method of creating dielectric profiles as in Eqn. 1, however, with a large dielectric contrast. The method can be implemented either using a multilayer deposition or standard lithographical techniques.

Recall that Eqn. 1 is actually a cosine series. Therefore, in general, we will have a DPS as long as the Fourier series of any periodic dielectric function, at least in an approximation, takes the form of Eqn. 1. Thus, what is really needed to form a DPS, is a dielectric function with two closely spaced frequency peaks (at frequencies G and G/r) in its’ spatial Fourier spectra.

Consider a dielectric profile, $\varepsilon_A(x)$ as in Fig. 7(a) which has a period a . This is a binary profile with alternating dielectric constants of ε_a and ε_b . The fundamental harmonic of $\varepsilon_A(x)$ occurs at the frequency $G = 2\pi/a$. In Fig. 7(b), we have a similar dielectric function $\varepsilon_B(x)$, but with a period ra . The fundamental harmonic $\varepsilon_B(x)$ is therefore, at the frequency $2\pi/ra = G/r$. Now if we linearly combine $\varepsilon_A(x)$ and $\varepsilon_B(x)$ as $\varepsilon(x) = 0.5\{\varepsilon_A(x) + \varepsilon_B(x)\}$ [see Fig. 7(c)] then by the linearity of the Fourier transform, the new function $\varepsilon(x)$ will have two Fourier peaks at frequencies G and G/r . Therefore to a good approximation this results in dielectric profile similar to Eqn. 1. Note that in Fig. 7(a,b), the dielectric functions are binary valued, however the dielectric function in Fig. 7(c) is not a binary profile. In order to implement this dielectric profile, we need three materials with dielectric constants ε_a , ε_b , and $0.5(\varepsilon_a + \varepsilon_b)$.

Although the linear combination looks simple in its’ operation, the real implementation requires a third material with the dielectric constant $0.5(\varepsilon_a + \varepsilon_b)$. This condition can be relaxed, if we use a logical combination, instead of the linear combination. The output of a logical combination is always binary, and therefore if we combined $\varepsilon_A(x)$ and $\varepsilon_B(x)$, using a logical operation at every x , then we will obtain a dielectric profile with the binaries ε_a and ε_b . Further, if we properly choose the duty cycle of $\varepsilon_A(x)$ and $\varepsilon_B(x)$, this will also give two strong harmonics at frequencies G and G/r . For an example in Fig. 7(a,b), assume the length of the ε_a portion within each period is $0.2a$. If we treat ε_a and ε_b to be equivalent to the binaries 1 and 0, and logically combine, $\varepsilon_A(x)$ and $\varepsilon_B(x)$, using a logical OR combination, then the result is the dielectric profile as shown in Fig. 7(d). The Fourier transform of this

dielectric profile is shown in Fig. 7(e) for $\varepsilon_a = 3.4$ (silicon) and $\varepsilon_b = 1.45$ (silicon dioxide). As we can clearly see, the Fourier transform exhibits two profound peaks at the frequencies G and G/r .

Therefore, using the method of linear and logical combinations, we can generate non-continuous, high dielectric contrast DPS structures. The dielectric profiles in Fig. 7(c,d) can be easily fabricated either via multilayer deposition, or lithographical techniques. One important point to note when handling high dielectric contrast logically or linearly combined structures is that their Fourier transforms will also consist of the higher order harmonics. Nevertheless, the continuous dispersion curve for the limit $r \rightarrow 1$ is still obtainable via exact numerical calculations, and the photonic harmonic oscillator theory will serve as a qualitative model that gives a good physical perspective.

Conclusion

In conclusion, we have presented the unique dispersion properties of a DPS with two closely spaced harmonics. Our discussion confirms that the anomalous dispersion of the DPS in the vicinity of ω_0 , is due to the linear perturbation in the dielectric function of the SPS. As we have shown, this linear perturbation is analogous to a presence of a harmonic oscillator, which pulls the light back towards the equilibrium position [i.e., $x = 0$ in Fig. 4(a), new coordinate system].

One of the key signatures of the DPS is the large density of flat bands with modes of Gaussian tails. This can be used designing high quality broadband, and multichannel slow light devices. The anomalous dispersion of the DPS also can be engineered to generate new class of passive superluminal, and dispersion controlling devices. Although we have presented the DPS in one dimension for an optical wave, the idea can be easily extended, to generate harmonic oscillators, and therefore lossless effective dispersive metamaterials, in higher dimensions, and other physical wave systems.

Methods

The continuous dispersion curve for the limit $R \rightarrow \infty$, and the photonic band structures for finite values of R are obtained using the plane wave expansion method²⁹. The continuous dispersion curve is obtained by increasing R to a huge value, until the results are converged. Specifically, in this paper we used $R = 10000$ to obtain the dispersion curve [Figs 2(a) and 4(d)]. The transmission spectra for the DPS are obtained using transfer matrix method (TMM)⁴³. In TMM simulations, we slice the continuous dielectric profile [Eqn. 1], into large number of spatial steps with uniform dielectric constants. We verified the TMM results independently, using the finite-difference time domain (FDTD)⁴⁴ simulation. For FDTD simulation we used the freely available software, MEEP⁴⁵.

References

1. K. J. Boller, A. Imamoglu & S. E. Harris, Observation of electromagnetically induced transparency. *Phys. Rev. Lett.* **66**, 2593–2596 (1991).
2. J. P. Marangos, Electromagnetically Induced Transparency. *J. Mod. Opt.* **45**, 471–503 (1998).
3. M. Fleischhauer, A. Imamoglu & J. P. Marangos, Electromagnetically induced transparency: Optics in coherent media. *Rev. Mod. Phys.* **77**, 633–673 (2005).
4. J. B. Khurgin, Slow light in various media: a tutorial. *Adv. Opt. Photonics* **2**, 287–318 (2010).
5. A. M. Steinberg & R. Y. Chiao, Dispersionless, highly superluminal propagation in a medium with a gain doublet. *Phys. Rev. A* **49**, 2071–2075 (1994).
6. L. J. Wang, A. Kuzmich & A. Dogariu, Gain-assisted superluminal light propagation. *Nature* **406**, 277–279 (2000).
7. A. Kuzmich *et al.* Signal Velocity, Causality, and Quantum Noise in Superluminal Light Pulse Propagation. *Phys. Rev. Lett.* **86**, 3925–3928 (2001).
8. R. W. Boyd & D. J. Gauthier, ‘Slow’ and ‘fast’ light. *Progress in Optics* **43**, 497–530 (2002).
9. R. Y. Chiao & P. W. Milonni, Fast Light, Slow Light. *Optics and Photonics News* **13**, 26–30 (2002).
10. S. Zhang, D. A. Genov, Y. Wang, M. Liu & X. Zhang, Plasmon-Induced Transparency in Metamaterials. *Phys. Rev. Lett.* **101**, 047401 (2008).
11. Y. Zhu, X. Hu, H. Yang & Q. Gong, On-chip plasmon-induced transparency based on plasmonic coupled nanocavities. *Scientific Reports* **4**, 3752 (2014).
12. D. D. Smith, H. Chang, K. A. Fuller, A. T. Rosenberger & R. W. Boyd, Coupled-resonator-induced transparency. *Phys. Rev. A* **69**, 063804 (2004).
13. Q. Xu *et al.* Experimental Realization of an On-Chip All-Optical Analogue to Electromagnetically Induced Transparency. *Phys. Rev. Lett.* **96**, 123901 (2006).
14. X. Yang, M. B. Yu, D. L. Kwong & C. W. Wong, All-Optical Analog to Electromagnetically Induced Transparency in Multiple Coupled Photonic Crystal Cavities. *Phys. Rev. Lett.* **102**, 173902 (2009).
15. A. Naweed, G. Farca, S. I. Shopova & A. T. Rosenberger, Induced transparency and absorption in coupled whispering-gallery microresonators. *Phys. Rev. A* **71**, 043804 (2005).
16. C. W. Hsu, B. G. DeLacy, S. G. Johnson, J. D. Joannopoulos & M. Soljačić, Theoretical criteria for scattering dark states in nanostructured particles. *Nano Lett.* **14**, 2783–2788 (2014).
17. Z. Ruan & S. Fan, Superscattering of Light from Subwavelength Nanostructures. *Phys. Rev. Lett.* **105**, 013901 (2010).
18. L. Verslegers, Z. Yu, Z. Ruan, P. B. Catrysse & S. Fan, From Electromagnetically Induced Transparency to Superscattering with a Single Structure: A Coupled-Mode Theory for Doubly Resonant Structures. *Phys. Rev. Lett.* **108**, 083902 (2012).
19. G. Alagappan & C. E. Png, Broadband slow light in one-dimensional logically combined photonic crystals. *Nanoscale* **7**, 1333–1338 (2015).
20. R. Shimada, T. Koda, T. Ueta & K. Ohtaka, Strong localization of Bloch photons in dual-periodic dielectric multilayer structures. *J. Appl. Phys.* **90**, 3905 (2001).
21. A. G. Yamilov & M. F. Bertino, Disorder-immune coupled resonator optical waveguide. *Opt. Lett.* **32**, 283–285 (2007).
22. S. Gasiorowicz, *Quantum Physics Third Edition* (John Wiley & Sons, 2003).
23. R. Y. Chiao, Superluminal (but causal) propagation of wavepackets in transparent media with inverted atomic population. *Phys. Rev. A* **48**, R34–R37 (1993).
24. R. Y. Chiao & J. Boyce, Superluminality, Pairelectricity, and Earnshaw’s Theorem in Media with Inverted Populations. *Phys. Rev. Lett.* **73**, 3383–3386 (1994).
25. E. Lorenzo *et al.* Porous silicon-based rugate filters. *Appl. Opt.* **44**, 5415–5421 (2005).

26. V. Kimberg *et al.* Angular properties of band structures in one-dimensional holographic photonic crystals. *J. Opt. A: Pure Appl. Opt.* **6**, 991 (2004).
27. C. S. Bartholomew *et al.* Rugate filters by laser flash evaporation of SiO_x N_y on room-temperature polycarbonate. *Journal of Vacuum Science & Technology A* **6**, 1703–1707 (1988).
28. J. Weber, H. Bartzsch & P. Frach, Sputter deposition of silicon oxynitride gradient and multilayer coatings. *Appl. Opt.* **47**, C288–C292 (2008).
29. K. Sakoda, *Optical Properties of Photonic Crystals* (Springer, 2001).
30. N. W. Ashcroft & N. D. Mermin, *Solid State Physics* (Thomson Learning Inc., 1976).
31. R. Y. Chiao & A. M. Steinberg, Tunneling Times and Superluminality. *Progress in Optics* **37**, 345–405 (1997).
32. G. Nimtz, On superluminal tunneling. *Progress in Quantum Electronics* **27**, 417–450 (2003).
33. S. Esposito, Universal photonic tunneling time. *Phys. Rev. E* **64**, 026609 (2001).
34. Ch. Spielmann, R. Szipöcs, A. Stingl & F. Krausz, Tunneling of Optical Pulses through Photonic Band Gaps. *Phys. Rev. Lett.* **73**, 2308–2311 (1994).
35. A. Yariv, Y. Xu, R. K. Lee & A. Scherer, Coupled-resonator optical waveguide: a proposal and analysis. *Opt. Lett.* **24**, 711–713 (1999).
36. J. D. Joannopoulos, S. G. Johnson, J. N. Winn & R. D. Meade, *Photonic Crystals: Molding the Flow of Light Second Edition* (Princeton University Press, 2008).
37. R. W. Boyd, *Nonlinear Optics Third Edition* (Elsevier Academic Press, 2008).
38. G. B. Arfken & H. J. Weber, *Mathematical Methods for Physicists Sixth Edition* (Elsevier Academic Press, 2005).
39. Y. Akahane, T. Asano, B. S. Song & S. Noda, High-Q photonic nanocavity in a two-dimensional photonic crystal. *Nature* **425**, 944–947 (2003).
40. J. Kasprzak *et al.* Bose–Einstein condensation of exciton polaritons. *Nature* **443**, 409–414 (2006).
41. M. Notomi, E. Kuramochi & T. Tanabe, Large-scale arrays of ultrahigh-Q coupled nanocavities, *Nat. Phot.* **2**, 741–747 (2008).
42. Q. Li, T. Wang, Y. Su, M. Yan & M. Qiu, Coupled mode theory analysis of mode-splitting in coupled cavity system, *Opt. Exp.* **18**, 8367–8382 (2010).
43. A. Yariv & P. Yeh, *Optical Waves in Crystals Third Edition* (John Wiley and Sons. Inc., 2003).
44. A. Taflov & S. C. Hagness, *Computational Electrodynamics: The Finite-Difference Time-Domain Method Third Edition* (Norwood, MA: Artech House, 2005).
45. Ardavan F. Oskooi, David Roundy, Mihai Ibanescu, Peter Bermel, J. D. Joannopoulos & Steven G. Johnson, MEEP: A flexible free-software package for electromagnetic simulations by the FDTD method, *Computer Physics Communications* **181**, 687–702 (2010).

Author Contributions

G.A. proposed the idea, performed the numerical simulations, and developed the theory. C.E.P. participated in the discussions and checked the results.

Additional Information

Competing financial interests: The authors declare no competing financial interests.

How to cite this article: Alagappan, G. and Png, C. E. Doubly Resonant Optical Periodic Structure. *Sci. Rep.* **6**, 20590; doi: 10.1038/srep20590 (2016).



This work is licensed under a Creative Commons Attribution 4.0 International License. The images or other third party material in this article are included in the article's Creative Commons license, unless indicated otherwise in the credit line; if the material is not included under the Creative Commons license, users will need to obtain permission from the license holder to reproduce the material. To view a copy of this license, visit <http://creativecommons.org/licenses/by/4.0/>